Solar Phys (2010) 265: 137–157
DOI 10.1007/s11207-010-9593-5

Ooty Interplanetary Scintillation – Remote-Sensing Observations and Analysis of Coronal Mass Ejections in the Heliosphere

P.K. Manoharan

Received: 1 February 2010 / Accepted: 11 June 2010 / Published online: 24 July 2010

Abstract In this paper, I investigate the three-dimensional evolution of solar wind density and speed distributions associated with coronal mass ejections (CMEs). The primary solar wind data used in this study has been obtained from the interplanetary scintillation (IPS) measurements made at the Ooty Radio Telescope, which is capable of measuring scintillation of a large number of radio sources per day and solar wind estimates along different cuts of the heliosphere that allow the reconstruction of three-dimensional structures of propagating transients in the inner heliosphere. The results of this study are: *i*) three-dimensional IPS images possibly show evidence for the flux-rope structure associated with the CME and its radial size evolution; the overall size and features within the CME are largely determined by the magnetic energy carried by the CME. Such a magnetically energetic CME can cause an intense geomagnetic storm, even if the trailing part of the CME passes through the Earth; *ii*) IPS measurements along the radial direction of a CME at $\sim 120\ R_{\odot}$ show density turbulence enhancements linked to the shock ahead of the CME and the core of the CME. The density of the core decreases with distance, suggesting the expansion of the CME. However, the density associated with the shock increases with distance from the Sun, indicating the development of a strong compression at the leading edge of the CME. The increase of stand-off distance between $\sim 120\ R_{\odot}$ and 1 AU is consistent with the deceleration of the CME and the continued outward expansion of the shock. The key point in this study is that the magnetic energy possessed by the transient determines its radial evolution.

Keywords Radio scintillation · Coronal mass ejections, initiation and propagation, interplanetary · Solar wind, disturbances, shock waves · Cosmic rays · Coronal holes

Remote Sensing of the Inner Heliosphere
Guest Editors: M.M. Bisi, and A.R. Breen.

P.K. Manoharan (✉)
Radio Astronomy Centre, National Centre for Radio Astrophysics, Tata Institute of Fundamental Research, Udhagamandalam (Ooty) 643001, India
e-mail: mano@ncra.tifr.res.in

1. Introduction

It has been recognized that coronal mass ejections (CMEs) are responsible for most of large geomagnetic disturbances at Earth (*i.e.*, disturbance storm time index, Dst ≤ -100 nT) and their associated adverse space weather effects (see, *e.g.*, Zhang *et al.*, 2007). Moreover, both CMEs and co-rotating interaction regions (CIRs) play a role in shaping the large-scale structure of the entire heliosphere and in determining the solar modulation of galactic and anomalous cosmic rays (see, *e.g.*, Tsurutani *et al.*, 2006; Hundhausen, 1977). Therefore, in the 'Sun – Earth connection' studies, major efforts are directed towards the identification and understanding of detailed structures and investigations of propagation and evolution of CMEs and CIRs in the entire inner heliosphere. Since *in-situ* measurements are limited and confined to the ecliptic plane, the remote sensing of the solar wind over a wide range of heliographic distances, longitudes and latitudes is expected to provide a better picture of the evolution of the heliosphere.

The interplanetary scintillation (IPS) remote-sensing technique can provide a global view of the solar wind (see, *e.g.*, Hewish, Scott, and Wills, 1964; Coles, 1978). IPS observations have also been useful to study the evolution of coronal transients (*e.g.*, CMEs) and development of solar wind disturbances (*e.g.*, CIRs) while these propagate through interplanetary space (see, *e.g.*, Purvis *et al.*, 1987; Manoharan *et al.*, 1995; Janardhan *et al.*, 1996; Manoharan *et al.*, 2001; Manoharan, Pick, and LASCO Consortium, 2002; Tokumaru *et al.*, 2003). In this paper, IPS data obtained at a radio frequency of 327 MHz from the Ooty Radio Telescope (ORT), located in the southern part of India, are utilized, supplemented with other space- and ground-based measurements, to study the evolution of CMEs, their shocks, the structures embedded within the CME, and their relationship to physical conditions on the Sun.

The paper is organized as follows: Section 2 gives a brief introduction of the Ooty Radio Telescope and discusses the IPS measurements made at Ooty. Section 3 describes the inner-heliospheric responses associated with propagation of CMEs. Section 4 analyzes the measurements from a CME along several lines of sight over time. Section 5 summaries the results.

2. The Ooty Radio Telescope and Interplanetary Scintillation Studies

The Ooty Radio Telescope (ORT) is a parabolic cylinder 530 m long in the north – south direction and 30 m wide in the east – west direction (see, *e.g.*, Swarup *et al.*, 1971). The unique design of ORT is that it has been constructed on a hilly slope of $\sim 11^\circ$ to compensate the northern geographical latitude of Ooty and the long axis of the telescope becomes parallel to the Earth's rotation axis. In this equatorial mount, a celestial radio source can thus be tracked for about ten hours by the mechanical rotation of the parabolic cylinder in the east – west direction. In the north – south direction, the telescope response is steered electronically by introducing a suitable phase and delay gradient along the 1056-dipole array (see, *e.g.*, Selvanayagam *et al.*, 1993). The present system supports the electronic steering of declinations between -60° and $+60^\circ$.

The ORT is equipped with a 12-consecutive simultaneous beam system, with a separation of ~ 3 arc min between adjacent beams. Since the size of the beam in the east – west direction is $\sim 2^\circ$, these 12 beams together can cover $2^\circ \times 36$ arc min of the sky area and thus provides an opportunity to observe more than one source at a given time. The switching of the beam from one direction to the other can be done within a few seconds. The high

sensitivity of the ORT helps to achieve a good signal-to-noise (S/N) with about 2 – 3 min integration time on a source. For example, ORT can detect a scintillation flux density of ~ 50 milli Jy (1 Jansky (Jy) $= 10^{-26}$ W m^{-2} Hz^{-1}), at a S/N ≥ 10 within an integration time of ~ 1 min. The high sensitivity and the fast switching of beams from one source to the other thus allows observations of a large number of radio sources in a day.

2.1. Interplanetary Scintillation

'*Interplanetary Scintillation*' (IPS) refers to the fluctuations in the intensity of a radio source caused by the combined effects of solar wind density irregularities, the rate at which these irregularities move perpendicular to the line of sight to the radio source, and the angular size of the source itself. Thus, an appropriate inversion of the suitably-sampled data might provide the solar wind density turbulence spectrum, velocity of the solar wind, and the angular extent of the brightness distribution of the source.

In general, the scintillation of a radio source can be quantified by the intensity fluctuations above its average intensity, which is defined by

$$\Delta I(t) = I(t) - \langle I(t) \rangle, \tag{1}$$

where $I(t)$ and $\langle I(t) \rangle$ represent, respectively, the intensity of the radio source at a given time, t, and the average level of source intensity. The degree of scintillation is given by the 'scintillation index', m = rms of intensity fluctuations normalized by the mean intensity of the source as given by

$$m = \left(\frac{\langle \Delta I(t)^2 \rangle}{\langle I \rangle^2} \right)^{\frac{1}{2}}. \tag{2}$$

The Fourier transformation of the auto-correlation function of the observed intensity fluctuations can yield the temporal power spectrum of the scintillation as given by

$$P(f) = \frac{1}{2\pi} \int_{-\infty}^{\infty} \rho(0, t) \exp(-\mathrm{i}2\pi f t)\, \mathrm{d}t, \tag{3}$$

where $\rho(0, t) = \langle \Delta I(0, t_0)\ \Delta I(0, t_0 + t) \rangle$ is the auto-correlation function of intensity fluctuations and f is the temporal frequency. Since the temporal spectrum is the integration of effects of solar wind over the $x - y$ plane as well as the summation along the line of sight, z, the temporal spectrum of scintillation can be represented as

$$P(f) = (2\pi r_\mathrm{e} \lambda)^2 \int_{\text{observer}}^{\infty} \frac{\mathrm{d}z}{|V_p(z)|} \int_{-\infty}^{+\infty} \mathrm{d}\kappa_y\, C_{N_\mathrm{e}}^2\, \Phi_{N_\mathrm{e}}(\kappa_x, \kappa_y, z) \times F_{\text{diff}}(\kappa_x, \kappa_y, z)\, F_{\text{source}}(\kappa_x, \kappa_y, z). \tag{4}$$

In the above equation, r_e is the classical electron radius and λ the wavelength of the observation. $F_{\text{diff}}(\kappa_x, \kappa_y, z) = 4 \sin^2(\kappa^2 z \lambda / 4\pi)$ is the Fresnel propagation filter. The Fresnel filter attenuates wavenumbers smaller than $\kappa_f \approx (2\pi/\lambda z)^{1/2}$ and does not alter the shape of temporal spectrum at large wavenumbers (*i.e.*, at small spatial scale lengths, $1/\kappa < 1/\kappa_f$) (Manoharan, Kojima, and Misawa, 1994). The spatial wavenumber is related to the temporal frequency, f, and the solar wind speed, V, as $\kappa = 2\pi f / V$. The term F_{source} is the

squared modulus of the radio source visibility function, given by $\exp[-(\kappa z \Theta_s/2.35)^2]$ for a symmetrical Gaussian brightness distribution of half maximum diameter, Θ_s and it cuts off the spectrum at wavenumbers above $\kappa_s = 1/(z\Theta_0)$. Therefore, as the size of the source increases, the scintillation gets quenched (Manoharan, 2006). The spatial spectrum of density fluctuations, power-law in nature, contains an inner-scale term, $\Phi_{N_e}(\kappa) = \kappa^{-\alpha} \exp(-\kappa^2/\kappa_i^2)$, where $S_i \approx 3/\kappa_i$ is the inner scale or cut-off scale of the turbulence and it is similar to the source-size cut-off. However, since almost all the sources have a size larger than the inner scale, the contribution of the inner scale is insignificant (Manoharan, Ananthakrishnan, and Rao, 1988; Manoharan, Kojima, and Misawa, 1994; Coles *et al.*, 1991; Chashei, 1997; Manoharan *et al.*, 2000; Yamauchi *et al.*, 1998).

It should also be noted that the scattering power in the solar wind (*i.e.*, the level of scintillation or the turbulence) falls of steeply with distance from the Sun, $C^2_{N_e}(R) \sim R^{-4}$ (Manoharan, 1993). In the case of solar wind flow without much of dominating structures of speed and/or density (*i.e.*, quiet solar wind), the line-of-sight integration of an IPS observation is therefore heavily weighted to the properties of the solar wind material at the closest point of the line-of-sight to the Sun (*i.e.*, the P-point). In such a situation, the P-point can be approximated as the point of IPS measurement. But when a solar wind transient crosses the line of sight other than its closest-solar-approach region and if it does not uniformly fill the entire line of sight, the P-point approximation leads to positional uncertainty in the measurement. However, as illustrated in the next section, when a large number of lines of sight of different positions and orientations with respect to the Sun are probed in a day, a computer-assisted tomography of such a data set allows one to remove the line of sight integration and the reconstruction of the three-dimensional heliosphere (see, *e.g.*, Kojima *et al.*, 1999).

For any given source, the scattering power increases as the Sun is approached and at a particular heliocentric distance, R_{peak}, it saturates (*i.e.*, $\Delta I(t) \approx \langle I \rangle$). Thus, the IPS measurements can be classified into two regimes, the weak-scattering heliosphere at $R > R_{\text{peak}}$ and the strong-scattering part at $R < R_{\text{peak}}$. The saturation radius, R_{peak}, is a function of observing frequency and it decreases with increasing frequency. For the ORT measurements at 327 MHz, the scintillation peaks at $R_{\text{peak}} \approx 40\ \text{R}_\odot$.

In the weak-scattering regime, ($R > 40\ \text{R}_\odot$), the scintillation index, m, is linearly related to the integral of $C^2_{N_e}(R)$ along the line of sight (Manoharan, 1993) and it is the integral of the temporal power spectrum. Therefore for a radio source of intensity $\langle I \rangle$, the scintillation index may also be given by

$$m^2 = \frac{1}{\langle I \rangle^2} \int_0^{f_c} P(f)\, \mathrm{d}f, \tag{5}$$

where f_c is the cut-off frequency of the temporal spectrum where the scintillation equals the noise level of the receiver system of the telescope. The temporal power spectrum, $P(f)$, can also be suitably calibrated (*i.e.*, using Equation (4)) to estimate the speed of the solar wind and shape of the density spectrum (Manoharan and Ananthakrishnan, 1990; Manoharan, Kojima, and Misawa, 1994). Further, the normalized scintillation, g, of a given source at a particular heliocentric distance is obtained by normalizing the measured scintillation index using the long-term average scintillation index (*i.e.*, the expected scintillation index) of the same source at the same heliocentric distance. Such a normalization removes the systematic variation of m with distance from the Sun and source-size effect (see, *e.g.*, Manoharan, 2006).

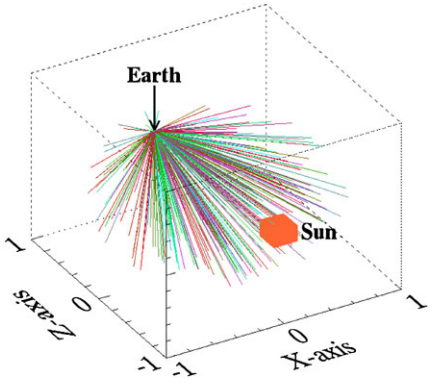

Figure 1 The three-dimensional view of lines of sight observed typically in a day (∼ 800) are shown. Each line corresponds to one radio source and its length represents the distance between the location of the observer (*i.e.,* Earth) to the point of closest solar approach of the line of sight (*i.e.*, the P-point). The location of the Sun is indicated by a square block.

3. Three-dimensional View of the Inner Heliosphere

Figure 1 shows the plot of lines of sight typically observed in a day at Ooty. In this three-dimensional plot, the length of each line indicates the distance between the Earth (*i.e.*, observer) and the P-point. The location of the Sun is shown by a square block. The figure illustrates that a considerable volume of the inner heliosphere is probed in a day. When measurements are taken on several consecutive days, these lines of sight tend to orient themselves around the Sun – Earth line and such observations are useful to obtain a global view of a large part of inner heliosphere. For example, in one solar rotation, the Ooty measurements cover a large number of lines of sight. These overlap with each other and thus they are able to provide the three-dimensional properties of solar generated disturbances. These include CMEs and co-rotating structures from the Sun to Earth orbit distances and beyond, and their interactions with each other as well as with slowly propagating structures of different sizes in the ambient background solar wind. For each IPS measurement, with sufficient spectral power, the fitting of the temporal power spectrum and the calibration of scintillation index yield, respectively, the velocity of the solar wind and the normalized scintillation index (g-value) (Manoharan, 2006; Manoharan and Ananthakrishnan, 1990).

The time-dependent computer-assisted tomography technique (CAT) developed at the University of California, San Diego, by B.V. Jackson and his team (see, *e.g.*, Jackson and Hick, 2005; Jackson *et al.* 2003, 2010) has been used to reconstruct the solar wind density and velocity. The basic data sets required for the three-dimensional reconstruction are the time series of velocity and g-value for a number of lines of sight of the heliosphere. For these studies, when both velocity and g-value are available for a given line of sight, they are included in the reconstruction analysis. The tomography technique forms a kinematic solar wind model at regular time intervals and iterates to provide the three-dimensional heliospheric parameters by fitting a model to the observed data (see, *e.g.*, Jackson *et al.*, 1998; Jackson and Hick, 2005; Hick and Jackson, 2004). For a given period of time (*e.g.*, one solar rotation), using the time-dependent tomography, the observations of the outward flowing material are combined to provide a three-dimensional reconstruction of the entire heliosphere at regular time intervals. Ooty IPS data observed during a period of high solar activity in solar cycle #23, October – November 2003, have been reconstructed in an earlier study and the comparison of reconstruction results with *in-situ* measurements has shown a good agreement (Bisi *et al.*, 2009).

3.1. Solar Events During 4 – 13 September 2005

The solar and interplanetary events that occurred during 4 – 13 September 2005 are studied based on Ooty IPS data obtained for distance ranges of the P-point from ∼ 40 to ∼ 250 $R_\odot$ and at all heliographic latitudes. In this period, most of the solar events considered had been associated with active regions (ARs) NOAA 10803 and 10808, which were separated by ∼ 150° on the solar disk. The former region, located close to the west limb of the Sun at the study period, produced mostly moderate flare/CME events of M-class and lesser intensity. However, these events were responsible for spectacular and orderly flux-rope type ejections, as illustrated following by the Ooty IPS analyses. Their expansion and propagation speed in interplanetary space was much faster than the ambient solar wind during the time period considered. Active Region 10808 produced a number of intense flare events and in fact, dominated the solar disk between 7 and 15 September 2005. For example, during the above period, AR 10808 produced 25 flares of intensity ≥ M-class, which included eight X-class flare events (http://www.ngdc.noaa.gov/stp/SOLAR/). However, in association with these intense flares only five full-halo CME events were observed (http://cdaw.gsfc.nasa.gov/CME_list/).

3.2. Ooty IPS Data – Three-dimensional Reconstruction

Figure 2 shows LASCO C2 white-light images of three CME events, which occurred on 4 – 6 September 2005. The parameters of these events are listed in Table 1. These CMEs show flux-rope-like structures in the LASCO field of view (see, *e.g.*, Krall and St. Cyr, 2006; Vourlidas *et al.*, 2000). In fact, the reconstruction of the Ooty IPS data shows the evolution and expansion of features that appear to be of flux-rope structures in the inner heliosphere. In Figures 3 to 5, the 3-D reconstructed heliospheric density is displayed for the period 8 – 13 September 2005, centered ∼ 0 UT for three different heliospheric views. Figure 6 shows velocity distributions for the same period. These 3-D constructions have been prepared from both density and velocity with spatial resolutions of 10° × 10° in latitude and longitude and temporal resolution of ∼12 hours at radial-distance intervals of 0.1 AU. The images of Figures 4 and 5 have been restricted to 3-D reconstructions in a latitude range of ± 50° in order remove dense structures not associated with the CMEs.

3.2.1. Density Maps and Remote-Observer Views

Figure 3 shows an ecliptic plane cut of the 3-AU diameter heliosphere as viewed from the north. In these plots, the orbit of the Earth is shown by a circle and the Earth is located to the right of its orbit (indicated by a ⊕ symbol). These one-day cadence cuts reveal several outward propagating features as well as co-rotating structures. For example, plots (a) to (e) show CME associated structures propagating to the western side of the Sun – Earth line. In these images, one can also see a fast-moving structure to the East of the Sun – Earth line, which is the interplanetary propagation signature of a possible fast halo CME that erupted from AR 10808 on 7 September 2005, at 17:40 UT, in association with an X17 flare event, which also produced a fast drifting Type II radio burst (speed ∼1900 km s^{-1}) (refer to event #4 in Table 1). Further, a co-rotating structure expanding with time can be seen in images (d) to (f) from behind the Sun (*i.e.*, ∼180° away from the Sun – Earth line). In these plots, only features in the ecliptic plane are viewed, and it is difficult to follow an individual event in the inner heliosphere. However, when the reconstructed data are plotted as a remote observer would view them for different orientations of the Sun – Earth line, they reveal the moving structures, corresponding to events on the Sun and their interactions in the inner heliosphere.

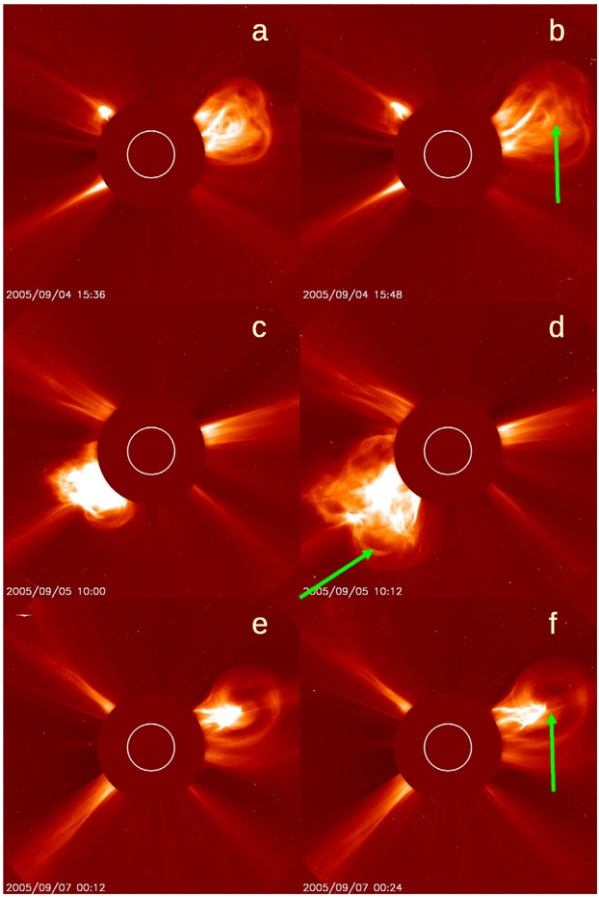

Figure 2 White-light images of three CMEs observed with the LASCO C2 coronagraph on 4 September (a and b), on 5 September (c and d), and on 7 September (e and f; these images show a CME that began on 6 September). Various parameters for these events are listed in Table 1 (events #1 to #3). The ejection of a flux rope is indicated by an arrow for each CME.

Table 1 Events marked in Figure 4 and their corresponding flare/CME parameters. The CME time refers to its onset at the LASCO C2 coronagraph. Events 1 to 3 are associated with the ejection of a prominence. For event #4 no LASCO data are available.

No.	Date	Flare Class	Flare Loc.	CME Time (UT)	CME Type	CME Speed $km\,s^{-1}$	PA	Type-II Speed $km\,s^{-1}$
1	04/09	C2.0	W Limb	14:48	PHalo	1000 – 1500	N – W	
2	05/09	C2.7	E Limb	09:48	Halo	2350	S – E	
3	06/09	M1.4	W Limb	21:12	PHalo	200 – 1000	N – W	
4	07/09	X17.0	S11E77	17:40	Halo?		S – E	$\geq$1900

Figures 4 and 5 show the three-dimensional remote-observer views of 3-D reconstructed heliospheric density from above the ecliptic plane. The orbit of the Earth is shown by a continuous-line ellipse. In Figure 4, the Earth is located to the right of each image, whereas in Figure 5, it is located to the left. These images combined with the ecliptic-plane plots (Figure 3) are useful to follow the three-dimensional evolution of propagating structures.

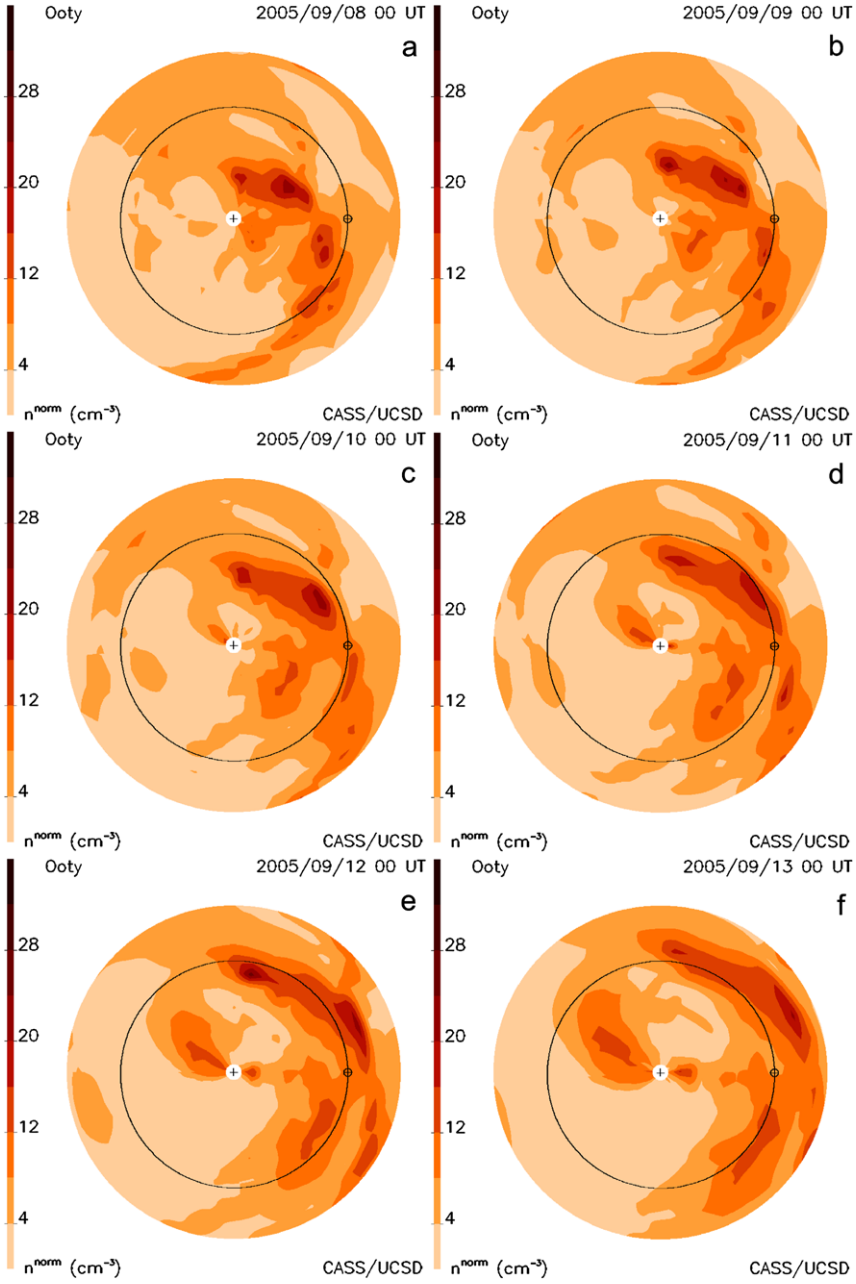

Figure 3 An ecliptic-plane density cut (viewed from the north) of the heliospheric density distribution obtained from the three-dimensional reconstruction of Ooty IPS measurements at 0 UT on each day from 8 to 13 September 2005. Each cut is 3 AU in diameter. The Sun is located at the center. The orbit of the Earth is shown by a circle and Earth is located at the right side of each image on its orbit. On the 9 September map (b) (also refer to Figure 6(b)), the interaction between low- and high-speed streams can be seen. The comparison of timings of these maps with *in-situ* measurements shows that the interaction has led to a shock at near-Earth space (refer to Figure 8). A CME following upstream of the interaction region crosses the Earth on 11 September 2005. Another CME and an interaction region are also observed on consecutive maps.

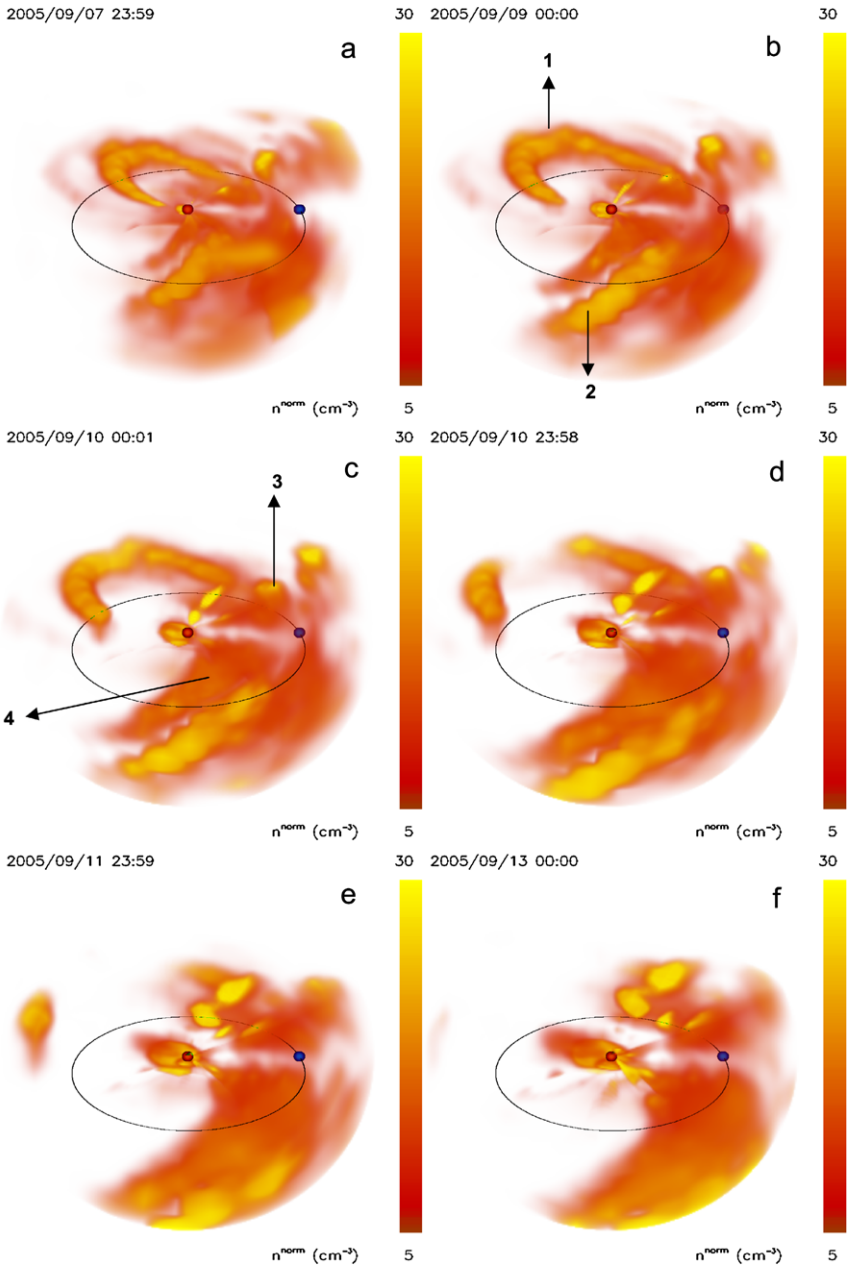

Figure 4 A three-dimensional remote-observer view of the heliospheric density obtained from the reconstruction of Ooty IPS measurements at ∼0 UT on days 8 to 13 September 2005. Each presentation covers a field of view of 3 AU and with the Sun located at the center. The orbit of the Earth is shown by an ellipse. In these plots, the observer is situated 30° above the Earth's orbit. The Earth is located to the right of each image (shown as a blue dot). In these maps, different solar wind disturbances can be observed to move outward. Flux-rope type features associated with the propagating CMEs can also be seen. The numbers indicated on the (b) and (c) plots correspond to events listed in Table 1. The numbers (1), (2), and (4) also indicate the flux-rope type features.

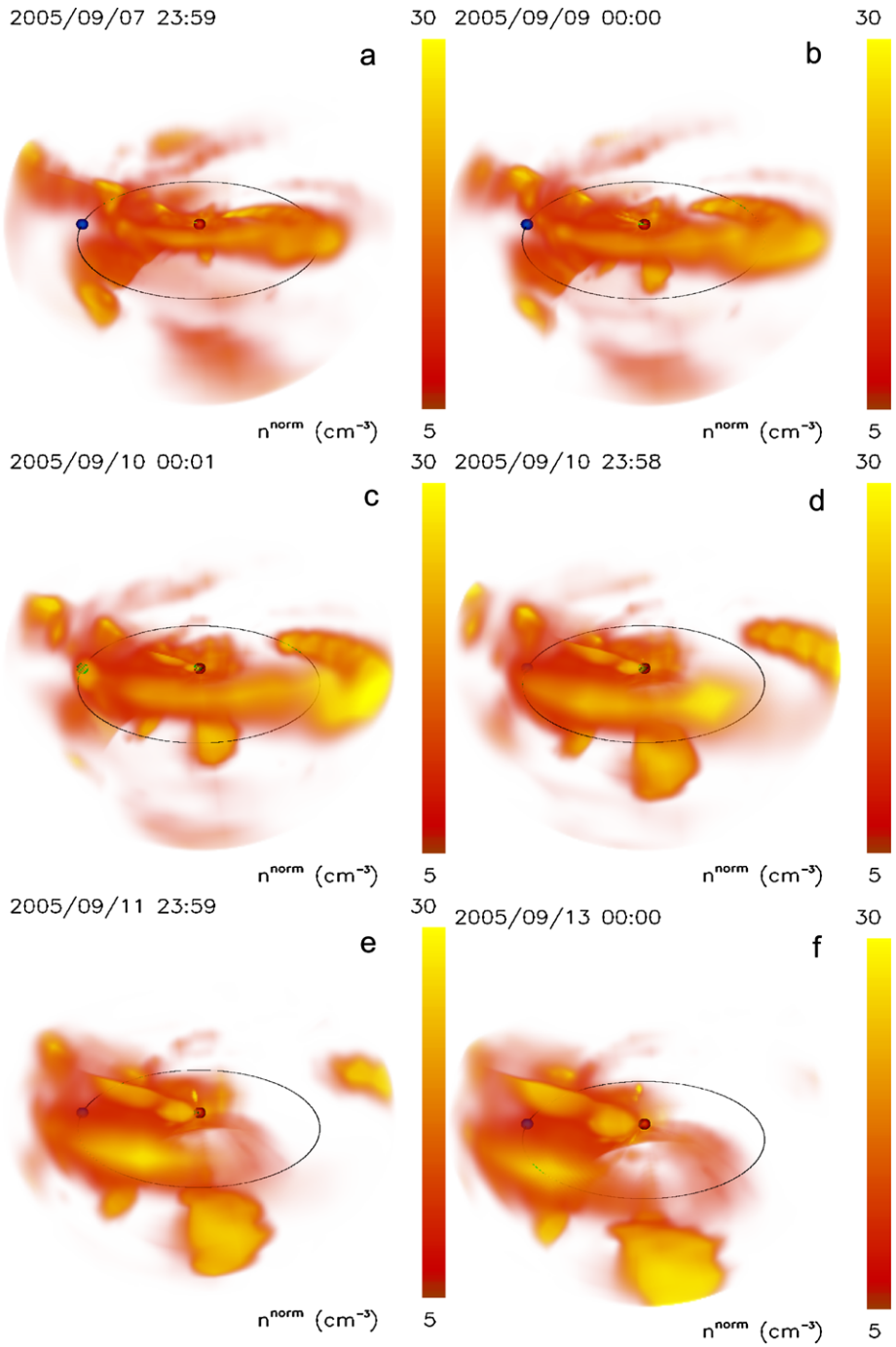

Figure 5 Same as Figure 4, but from a different viewing direction. The observer is located $\sim 30^\circ$ above the ecliptic plane and $\sim 90^\circ$ west of the Sun – Earth line.

In Figure 4, the loop-like features observed in north-western direction to the Sun – Earth line correspond to the CME event on 4 September 2005, at 14:48 UT (refer to LASCO C2 images shown in Figure 2 ((a) and (b) plots); event #1 in Table 1). The numbers marked in Figure 4 ((b) and (c)) correspond to events listed in Table 1. The event on 5 September at 09:48 UT also shows a long flux-rope structure in the east of the Earth (refer to event #2 in Table 1). The initial speed of the CME in the LASCO field of view was fast, ~ 2350 km s^{-1}. The event on 6 September 2005, at 21:12 (refer to event #3 in Table 1) was narrow and gradually accelerated in the LASCO field of view. Also, in the IPS field of view the size of this event shows only limited expansion.

The full set of reconstructed images (also refer to the movie stored online at the journal website) show the expansion of fast/slow moving structures associated with these events. The circular rim features observed can be interpreted as outlining flux-rope structures (refer to Figure 4(b) and (c)). In these cases, the overall size evolution of the CME (*i.e.*, diameter of the flux-rope type structure) in the Sun – 1-AU dimension follows a simple relationship, $L_{\mathrm{CME}} \sim R^{1.0}$ (Manoharan *et al.*, 2000). This shows that the internal pressure of the CME is higher than the ambient solar wind (see, *e.g.*, Gosling, 1997); the CMEs expand with distance from the Sun and maintain a dynamical equilibrium (*i.e.*, pressure balance) with the ambient solar wind. The internal pressure of the CME includes both the magnetic pressure and gas pressure. However, the thickness of the flux-rope type feature is smaller than the overall size of the CME and it does not change in linear relation with its overall size increase. In general, the extreme ultra-violet images of CME eruptions observed with the EIT show that the thickness of the flux rope (*i.e.*, erupting prominence/filament) is much smaller than the overall size of the CME observed in the LASCO C2 field of view (see, *e.g.*, Dere *et al.*, 1997). It is noted that the magnetic field of a flux rope at a distance R from the Sun is given by $B_{\mathrm{axial}}(R) + B_{\mathrm{azimuthal}}(R)$, where $B_{\mathrm{axial}}(R) = B_0 \exp(-R^2/a^2)$, $B_{\mathrm{azimuthal}} = (R/a)B_{\mathrm{axial}}$, and a is the radius of the flux rope; $B_{\mathrm{azimuthal}}$ can take a negative (left-handed field) or positive (right-handed field) (see, *e.g.*, Mulligan *et al.*, 2001). The present study suggests that the flux rope that erupted from the Sun expands with distance, but retains its shape up to 1 AU or beyond, and the magnetic internal energy possessed by the CME (or magnetic cloud) essentially determines the unwinding of fields and/or the expansion of the CME in the course of its propagation. The Ooty results are consistent with the study in that the flux-rope types of the CMEs are magnetically driven (see, *e.g.*, Mulligan *et al.*, 2001; Vourlidas *et al.*, 2000).

3.2.2. Velocity Ecliptic Cuts

The reconstructed density analyses compared with the corresponding velocity analyses are helpful to clearly follow the interplanetary features and interacting structures. Figure 6 displays the ecliptic velocity cuts corresponding to density plots displayed in Figure 3. In particular, the combination of velocity and density analyses are essential to understand the effects of solar and interplanetary disturbances at the near-Earth environment or elsewhere, *e.g.*, at Mars or other planetary systems. A careful comparison of heliospheric density and velocity from IPS as well as *in-situ* data (refer to Figures 3(b) and 6(b)) reveals a compression between a low-speed (high-density) stream and high-speed (low-density) wind from a coronal hole at distances near 1 AU. The location of this coronal hole near the equatorial region of the Sun can be seen in a sample He I 10 830 Å spectroheliogram observed on 9 September 2005, along with a comparison TRACE image at 171 Å observed on 2 September 2005, shown in Figure 7. The coronal hole appears dark in the TRACE EUV image. This interaction between the low-speed wind and high-speed stream resulted in a strong shock at 1 AU on 9 September (day number 252). Figure 8 shows *in-situ* measurements of solar wind plasma parameters and magnetic field. It also includes a geomagnetic index plot.

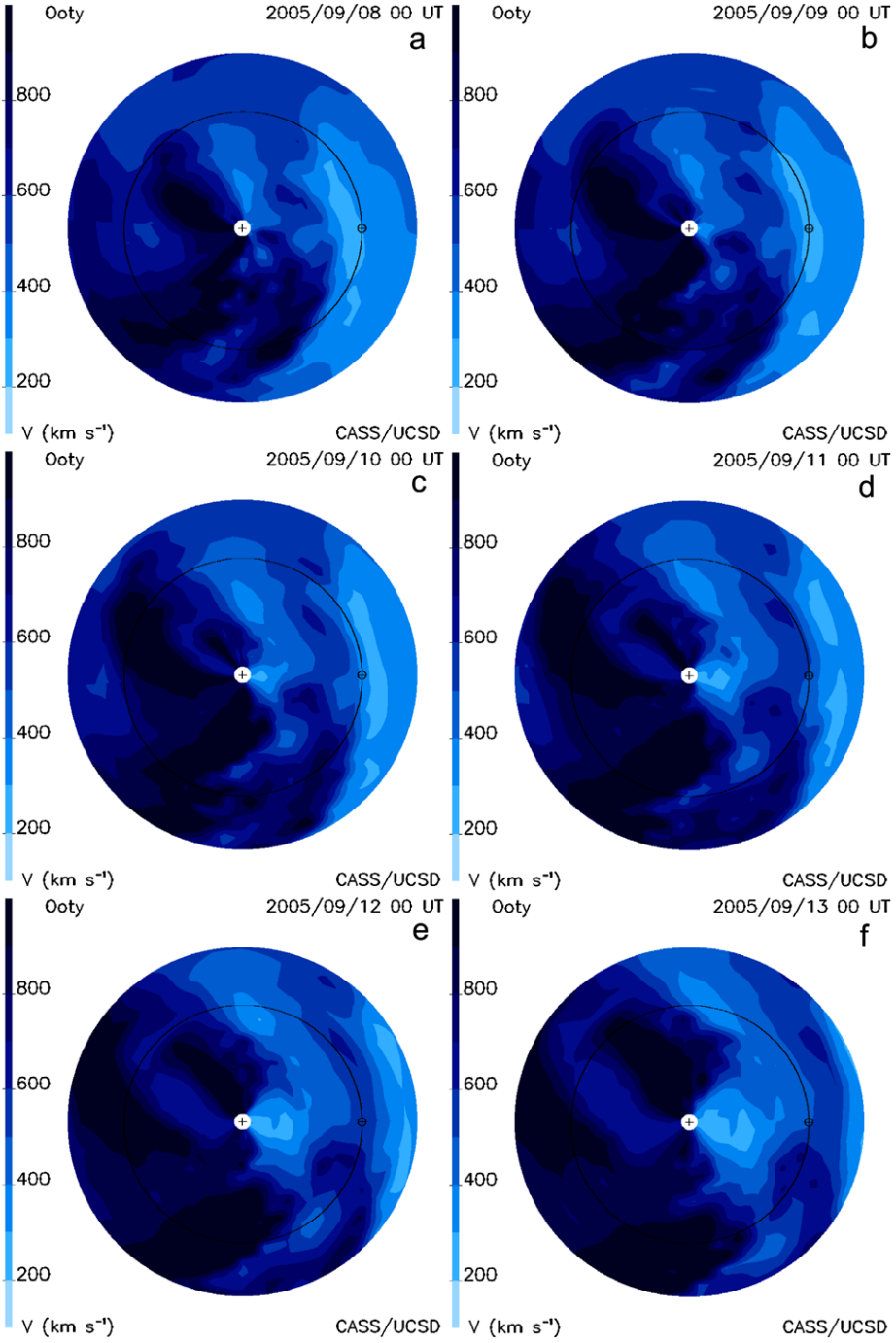

Figure 6 Same as Figure 3; shown is the velocity distribution of the heliosphere in the ecliptic plane, during 8 – 13 September 2005. On the 9 September plot ((b); also refer to Figure 3(b)), the interaction between low- and high-speed streams can be seen. This resulted in a shock on 9 September 2005 at Earth (refer to Figure 8).

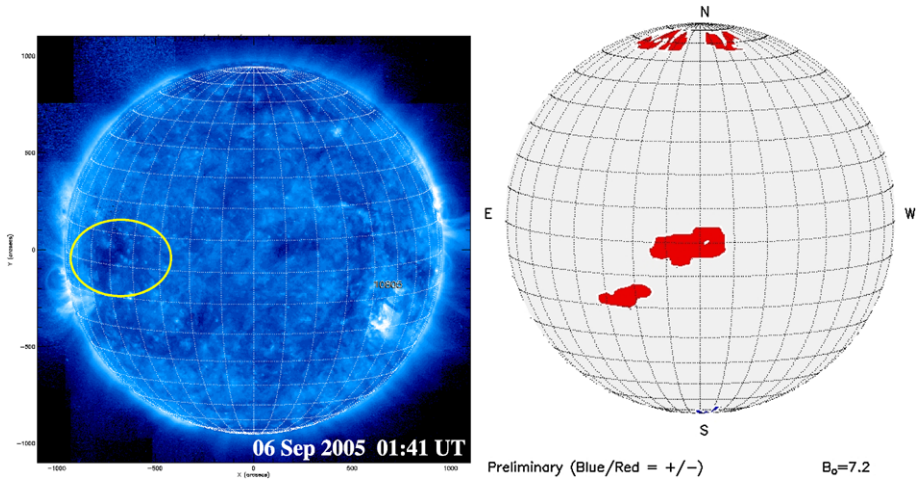

Figure 7 Full-disk TRACE 171 Å image obtained on 6 September 2005 (left). The coronal hole appears dark in the TRACE EUV image. The location of the coronal hole is indicated by an ellipse at the East. He I 10 830 Å map on 9 September 2005, from SOLIS data (right). The coronal hole has moved to the center of the disk (refer to Section 3.2.2).

Another interesting point is that the high-speed wind is followed by a fast-moving CME event associated with the flare on 7 September 2005, at 17:40 UT. Although this event originated at the eastern side of the disk (S11E77), it expanded to a large size and the western side of the CME passed through the Earth, causing an intense shock as well as a strong geomagnetic storm (Dst ∼150 nT). The solar wind interaction and CME events in the period under study caused four interplanetary shocks at the Earth. Their arrival times are indicated by vertical dotted lines in Figure 8. Since the solar events on or after 7 September 2005, occurred on the eastern side of the solar disk, their effects at the Earth have been mainly due to the west side of the shock and CME. Although the shocks have large strengths, except for the event during the early hours of 11 September (refer to event #2, Table 1), they produced only weak geomagnetic storms (refer to Figure 8).

4. Intense Flare/CME Event on 13 December 2006

An intense flare/CME event occurred in the active region NOAA AR 10930 (S06W23) on 13 December 2006, at 02:40 UT. It was an X3.4 event and also produced a Ground-Level Enhancement (GLE). (Normally a GLE event is associated with a powerful flare and it is identified by the percentage of enhancement of the neutron detector count above the background level.) In fact, this flare is one of the largest flares that occurred during the minimum phase of Solar Cycle 23. Multi-wavelength data obtained from the *Hinode* space mission (see, *e.g.*, Kubo *et al.*, 2007) have revealed the rotation and collision of two sunspots that led to the twisting and reconnection of magnetic fields in the corona and the launch of a fast CME directed towards the Earth (Su *et al.*, 2007; Liu *et al.*, 2008). Because of the prior knowledge of the onset of this CME, obtained from the LASCO webpage (ftp://lasco6.nascom.nasa.gov/pub/lasco/status/LASCO_CME_List_2006), a special mode of IPS '*picket-fence*' observation was initiated at Ooty to probe the CME in high-temporal resolution along the propagation direction of the CME.

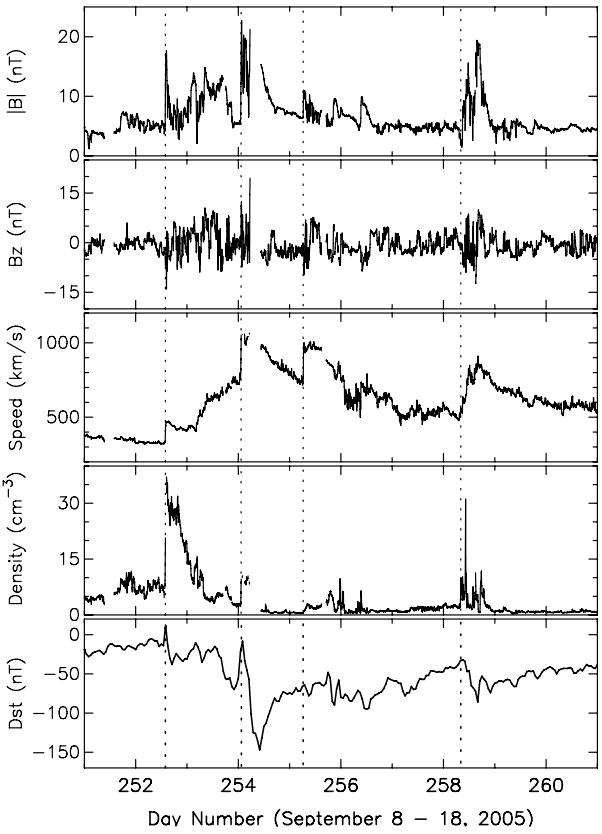

Figure 8 Plots of the interplanetary magnetic field (|**B**|, and B_z component), solar wind speed and density measurements at 1 AU, and ground-based geomagnetic storm data, for the period between 8 and 18 September 2005. This period includes four shocks and are intense enough to moderate geomagnetic storms. The vertical dotted lines mark the arrival times of shock at 1 AU. The first shock on 9 September 2005 has been produced by the interaction of low- and high-speed streams and the second one in the early hours of 11 September 2005 has resulted from the interaction between the high-speed stream and the fast-moving CME (refer to event #2 in Table 1).

4.1. Picket-Fence IPS Observing

The 'picket-fence' observation mode refers to a special type of observation in which only a few IPS sources (*i.e.*, lines of sight) are selected such that they lie at the expected location of the outward propagating CME and its associated interplanetary disturbance. The continuous monitoring of these sources at frequent intervals provides a number of measurements of the properties of

i) The ambient solar wind before the arrival of the disturbance at the IPS line of sight.
ii) The plasma along a radial cut through the shock, sheath, and CME.
iii) The upstream flow behind the disturbance.

Such IPS measurements, although integrated along a line of sight, are useful to study the characteristics of the plasma within the CME and the solar wind moving ahead and behind the disturbance. In this example, for the investigation of the present event, three sources were monitored; two sources, 1453-358 and 1453-109, were observed on 14 December and another source, 1245-197 on 14/15 December 2006. The sources, 1453-358 and 1245-197, have been chosen such that they are located at the western side of the Sun, respectively, at solar elongations $\sim 35^\circ$ ($R \approx 120$ R$_\odot$) and $\sim 60^\circ$ ($R \approx 190$ R$_\odot$) and their respective P-points at position angles (PAs) $\sim 240^\circ$ and $\sim 255^\circ$. These lines of sight correspond to

Earth – Sun – P-point angles of 55° and 30°. We assume that the leading edge of the disturbance is nearly spherical in shape centered at the Sun (see, *e.g.*, Howard *et al.*, 2007). With this assumption, since the CME is wide (*i.e.*, halo CME) and its originating location on the Sun is west, 23°, the disturbance will pass through the line of sight P-points at the same times as their outermost extremities and the timings determined by the line of sight crossings indicate an accurate relative outward propagation of the disturbance. The line of sight of the source, 1453-109, at a solar elongation of 37° and PA ∼ 280° (*i.e.*, ∼ 40° north of 1453-358) was chosen to provide information about the north-western extremity of the CME disturbance.

4.1.1. Interplanetary Structures of the CME

Figure 9 displays the overall summary and results of the special mode of observing. The LASCO white-light image, taken at 02:54 UT shows the CME onset in the C2 field of view. The linear speed of the CME obtained from the LASCO height – time plot is ∼1775 km s^{-1} at distances ≤ 20 $R_\odot$. Since the initiation location of the CME is close to S06W23, its speed along the south–west direction is likely to be less affected by the plane-of-sky projection. Moreover in this study, the LASCO speed has been employed to indicate the fast propagation of the event and hence no attempt has been made to correct the projection effect in the speed (see, *e.g.,* Michalek *et al.*, 2004). Two arrows plotted on the LASCO image (blue and green arrows) indicate, respectively, the position angles of radio sources, 1453-358 (PA = 240°) and 1453-109 (PA = 280°). As is evident, the position angle of 1453-358 probes the central part of the CME, whereas the other source (1453-103) would cross the CME's north-western extremity. As discussed in Section 2, these IPS observations are line-of-sight integrated, which is likely to cause an underestimation in the speed up to ∼10% (Manoharan, Kojima, and Misawa, 1994) as well as an uncertainty in the position of the CME. However, in this study, in order to avoid large positional errors, the propagation direction and selection of sources have been carefully matched, such that the crossing of the CME occurs near to the closest solar approach of the lines of sight to the above radio sources. The percentage of reduction in the speed caused by the line-of-sight integration will be nearly the same for all these measurements.

In Figure 9, the plots to the left show the normalized scintillation index (g-value) and solar wind speed observed on 14 December 2006, between 0 – 10 UT. Both g-value and speed plots show fluctuations as the CME crosses the lines of sight. Along the direction of the source 1453-358 at R = 120 $R_\odot$ and PA = 240°, an enhancement in g-value is observed at two time intervals separated by ∼ 2.5 hours. The first broad peak centered around 03:45 UT is likely caused by the shock (*i.e.*, the region between the shock and the driver CME). Since the speed of the CME was much larger than the background solar wind (∼1775 km s^{-1}), the corresponding first enhancement (presumably the shock) is observed to move approximately at the onset speed of the CME. The second enhancement observed in g-value at 06:45 UT shows a steep rise and it is likely due to the CME driver. An interesting point is that the density turbulence within the CME is greater than that within the shock-sheath region. The observed increase in density near the central portion of the CME (source 1453-358) is higher than the enhancement observed in the trailing portion of the CME (source 1453-109). It is likely that the compression and formation of a shock in the trailing portion is less effective in providing high g-values than in the central part of the CME.

The speed plot for the central part of the CME, probed by the source 1453-358, suggests an overall high speed of 1000 – 1500 km s^{-1} during the CME passage, and several peaks are seen in the speed profile. In the case of the line of sight to the north-western side of

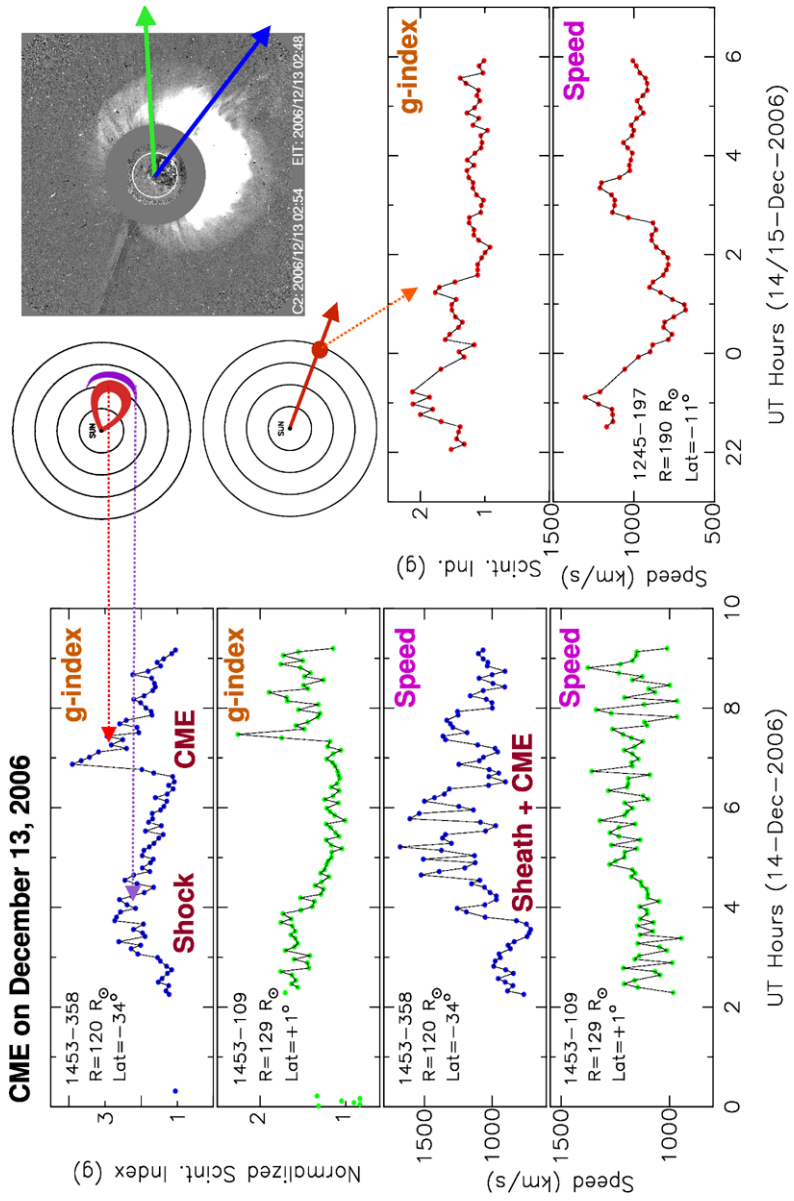

Figure 9 "Picket fencing" of the CME beginning on 13 December 2006, along three different IPS lines of sight. The left panel shows the *g*-value and speed observed on 14 December 2006, while the CME and its corresponding shock crossed the lines of sight of radio sources, 1453-358 and 1453-109, respectively, probing heliocentric distances of the P-point of 120 and 129 $R_{\odot}$. The position angles of these two radio sources, 240° and 280°, are indicated by arrows on the LASCO/SOHO C2 white-light image, which corresponds to the onset time of the CME at the C2 field of view on 13 December, at 02:54 UT. One of the concentric-circle diagrams shows the typical geometry of the interplanetary CME and its preceding shock. The other concentric-circle diagram and the right panel display the picket fencing of the CME at a large heliocentric distance, 190 $R_{\odot}$ a day following.

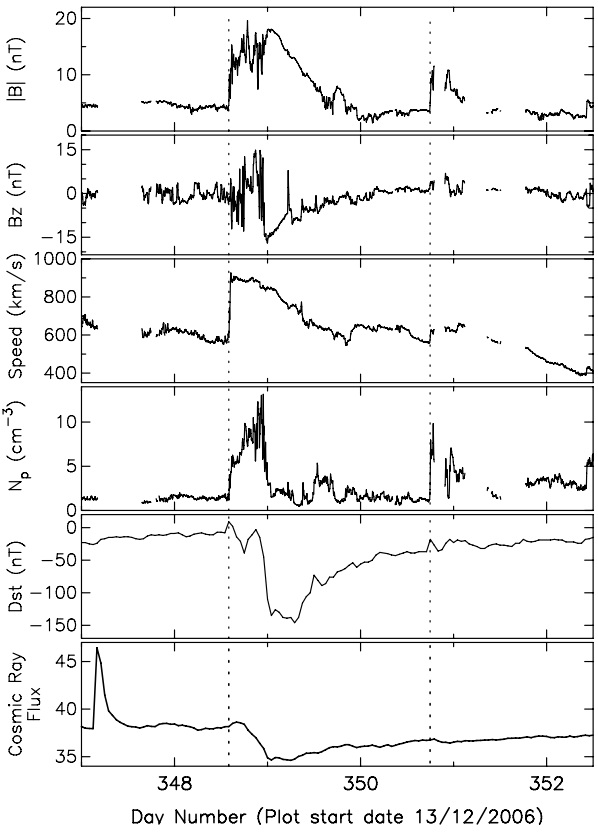

Figure 10 Near-Earth observations of interplanetary CME and the shock associated with the CME event on 13 December 2006. The top two panels show the magnetic-cloud properties and background solar wind observed (average field and B_z component). The middle two panels show the variations of solar wind speed and density. The bottom panels are ground-based observations of the geomagnetic storm index and the cosmic-ray intensity. A spike seen in the cosmic-ray flux shows the intensity of the ground-level enhancement at the onset of the CME/flare at 02:41 UT on 13 December 2006. The vertical line on 14 December indicates the arrival of an intense shock driven by the CME event. As indicated in the plot, the magnetized plasma in the sheath region (*i.e.,* between the shock and the CME) shows large variations, suggesting compressed plasma and amplification of the magnetic field in this region.

the CME (source 1453-109), the observed speed is $\sim$1200 km s^{-1}. The speed range at the central part of the CME suggests a possible stand-off distance (*i.e.*, distance between the shock and the driver gas) of ~ 20 R$_\odot$. The diagram of the CME geometry and the preceding shock is shown in a Sun-centered plot at the right side of the g-value plot in Figure 9.

In the following time interval (between 22 UT on the 14th and 7 UT on 15th of December), the line of sight for the source 1245-197 probed the heliocentric distance $\sim$190 R$_\odot$ and PA $= 255°$. The geometry and the position angle (refer to the red arrow on the plot) of this observing setup is shown in a Sun-centered plot. At this large distance, the level of turbulence (g-level) in the CME driver is lower than along the 120 R$_\odot$ line of sight. However, in the sheath region the turbulence is high. This suggests that the expansion within the CME leads to a decrease in density as well as density turbulence. An interesting point is that the CME speed is well above the ambient solar wind plasma ($\sim$1000 km s^{-1} at 190 R$_\odot$). At this distance, the interplanetary CME can be identified by its speed and this is consistent with *in-situ* measurements at 1 AU.

Figure 10 displays the solar parameters measured at 1 AU. This plot also includes profiles of geomagnetic index and cosmic-ray flux intensity observed from ground-based stations, respectively, the World Data Center for Geomagnetism, Kyoto University and the Cosmic ray Neutron Monitoring Station, Calgary. The large spike seen in the cosmic-ray flux plot is the GLE event due to the onset of the flare/CME at 02:40 UT on 13 December 2006. As shown in the solar wind plots, the CME event produced a strong shock and its arrival

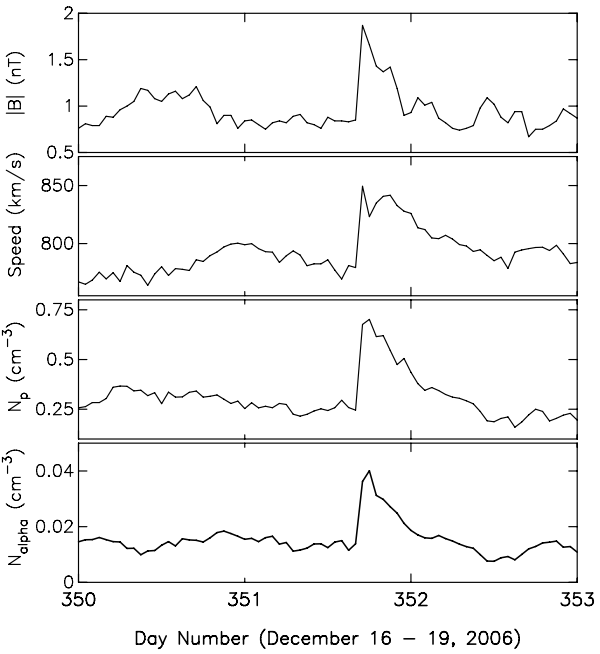

Figure 11 The arrival of the CME and its related disturbance at the orbit of *Ulysses* located at 2.7 AU, heliographic latitude −74°, and longitude ∼35°. These measurements suggest that the CME has expanded more than 1 AU in radial extent between the Sun and the *Ulysses* distance.

at 14:05 UT on 14 December is shown by the vertical dotted line. The interplanetary CME speed is ∼900 km s^{-1} at 1 AU, and this is consistent with the IPS measurements at a distance of 190 $R_\odot$ (∼1000 km s^{-1}). Moreover, the solar wind parameters in the sheath region show large fluctuations as observed in the IPS lines-of-sight time series. The time difference between the arrival times of the shock and the magnetic cloud of the CME suggests a stand-off time ∼10 hours (*i.e.*, ∼40 $R_\odot$), which is about two times larger than that observed at ∼120 $R_\odot$. The stand-off time (or distance) tends to increase as the CME slows down. The average magnitude of the field and its southward component (B_z) indicate that most of the field is oriented southward and caused an intense geomagnetic storm, Dst ∼ –147 nT. The magnetic cloud also produced a Forbush decrease in the cosmic-ray intensity of ∼8%, suggesting that the magnetic cloud engulfed the Earth.

Figure 11 shows the solar wind parameters measured at *Ulysses*, situated at a heliocentric distance of ∼2.7 AU, heliographic latitude −74° and longitude ∼35°. *Ulysses* was located ∼40° south of P-point of the radio source 1453-358. On 14 December, when the CME crossed the lines of sight of 1453-358 and 1453-109, the heliographic longitude of the P-point of these sources was in the range ∼55 – 60° and the line of sight of source 1453-109 was located ∼40° north in PA of that 1453-358. That is, at a heliocentric distance of ∼125 $R_\odot$, the CME likely expanded to an angular width of about 80°. In the LASCO field of view, the expansion of the CME was linearly proportional to the radial distance and a size of ∼15 $R_\odot$ was observed at a solar offset of ∼15 $R_\odot$. These facts and the enhanced alpha particle abundance (see, *e.g.*, Torsti *et al.*, 2001; refer to Figure 11) suggest that the CME expanded to a radius of >1 AU at the orbit of *Ulysses*.

The IPS picket-fence study of the CME provides evidence that the density turbulence embedded within the CME is large at a solar offset of ∼120 $R_\odot$ and tends to decrease at with distance. Since the solar wind density is related to its turbulence level (see, *e.g.*, Manoharan, 1993; Asai *et al.*, 1998), the large density observed at the small solar offset is in agreement

with the high-density core (*i.e.*, eruptive filament/prominence) observed in several CMEs (see, *e.g.*, Koutchmy *et al.*, 2008). The expansion of the CME leads to a gradual decrease in the density of the core. However, the density associated with the shock, moving in front the CME driver, gradually increases with distance from the Sun and this is consistent with an increasing shock compression and steepening ahead of the leading edge of the CME (*i.e.*, the driver) with distance. The size evolution of the CME with radial distance indicates that the CME size increases to larger than 1 AU at heliocentric distances outside the orbit of the Earth (Manoharan, 2006).

5. Summary

The remote-sensing IPS technique is extremely useful for a detailed study of CMEs and quiet solar wind in the three-dimensional heliosphere. In particular, when a large number of scintillators are employed to probe the solar wind, as discussed in Section 3, it provides a better understanding of the Sun – Earth relationship. The flux-rope type CME structures observed in the inner heliosphere provide evidence that the eruptive filament/prominence ejected from the Sun retains its shape even at large solar distances, suggesting that the magnetic energy associated with a CME is important to carry it intact to a large distance from the Sun. This is consistent with the ideas that

i) The magnetic helicity of a flux rope is conserved (*see, e.g.*, van Driel-Gesztelyi *et al.*, 2000).
ii) The magnetic pressure inside the magnetic cloud is higher than the gas pressure (see, *e.g.*, Burlaga, 1995).
iii) The characteristics of a magnetic cloud show a better fit with a non-force-free model (see, *e.g.*, Cid *et al.*, 2002).
iv) We have supportive evidence that the axial magnetic field is slightly lower than the azimuthal field even at large distances from the Sun at $R > 1$ AU (see, *e.g.*, Mulligan *et al.*, 2001).
v) Flux-rope CMEs are magnetically driven (see, *e.g.*, Vourlidas *et al.*, 2000).

These characteristics allow a flux rope shape to be maintained as the CME moves further out in the heliosphere as well as allow these magnetically energetic events to move outward against the force applied by the ambient background solar wind without losing their shape. In such a magnetically energetic CME, even if the center part of the CME is not crossing the Earth, the extremity of the CME may produce a considerably strong shock and geomagnetic storm at the Earth's magnetosphere. As discussed in Section 3, the pressure balance maintained between the CME and the ambient solar wind largely governs the expansion of the CME with distance.

The CME study using the IPS picket-fence method provides evidence that the density turbulence (also density) embedded within the CME is large at small solar offsets and tends to decrease at large solar distances. In the case of a fast CME, the shock is formed within $\sim$100 $R_\odot$. However, the compression tends to increase with distance. The compression and/or steepening at the center of the CME is more effective at providing a g-level enhancement than its trailing part. The doubling of the stand-off distance between $\sim$120 $R_\odot$ and 1 AU is consistent with the deceleration of the CME in this distance range (see, *e.g.*, Manoharan, 2006). The IPS observations are vital to understand the energy of the solar wind as well as the energy transfer between the disturbance and the surrounding ambient solar wind. This study emphasizes the importance of the magnetic energy in shaping the

transients and heliosphere. The combination of IPS images, SMEI, and white-light images from the current STEREO mission measurements would provide insight and a more complete view of the solar wind dynamics and their space weather effects.

Acknowledgements The author thanks the observing/engineering team and research students of Radio Astronomy Centre for the help in making observations and preliminary data reduction. The author thanks B.V. Jackson and his UCSD team for the IPS tomography analysis program. The author acknowledges the coronal and photospheric data provided by the Wilcox Solar Observatory (http://wso.stanford.edu). The hourly averaged interplanetary plasma and magnetic field data sets have been obtained from the NSSDC OMNIWeb Service maintained at http://nssdc.gsfc.nasa.gov/omniweb. The author acknowledges Kitt Peak Observatory for the magnetic field data, Kyoto Observatory for the geomagnetic data, and *Ulysses* team for the solar wind data. The LASCO images and data are courtesy of the SOHO consortium. The CME catalogue is maintained at http://cdaw.gsfc.nasa.gov/CME_list/. The EUV image is from TRACE mission of the Stanford-Lockheed Institute for Space Research, and part of the NASA Small Explorer program The SOLIS data used here have been produced cooperatively by NSF/NSO and NASA/LWS. The author also thanks S. Shaheda Begum for formatting some of the figures and for help with preparing the list of references. A part of this work was presented at the workshop on 'Remote Sensing in the Inner Heliosphere', held in Aberystwyth, Wales, 5 – 7 May 2009 and the author acknowledges the travel support to attend the workshop. This work is partially supported by the CAWSES – India Program, which is sponsored by the Indian Space Research Organisation (ISRO).

References

Asai, K., Kojima, M., Tokumaru, M., Yokobe, A., Jackson, B.V., Hick, P.L., Manoharan, P.K.: 1998, *J. Geophys. Res.* **103**, 1991.

Bisi, M.M., Jackson, B.V., Clover, J.M., Manoharan, P.K., Tokumaru, M., Hick, P.P., Buffington, A.: 2009, *Ann. Geophys.* **27**, 4479.

Burlaga, L.F.: 1995, *Interplanetary Magnetohydrodynamics*, Oxford University Press, New York.

Chashei, I.V.: 1997, *Adv. Space Res.* **12**, 2299.

Cid, C., Hidalgo, M.A., Nieves-Chinchilla, T., Sequeiros, J., Vinas, A.F.: 2002, *Solar Phys.* **207**, 187.

Coles, W.A.: 1978, *Space Sci. Rev.* **21**, 411.

Coles, W.A., Liu, W., Harmon, J.K., Martin, C.L.: 1991, *J. Geophys. Res.* **96**, 1745.

Dere, K.P., Brueckner, G., Howard, R.A., Koomen, M.J., Korendyke, C.M., Kreplin, R.W., Michels, D.J., Moses, J.D., Moulton, N.E., Socker, D.G.: 1997, *Solar Phys.* **175**, 601.

Gosling, J.T.: 1997, In: Crooker, N., Joselyn, J.A., Feynman, J. (eds.) *Coronal Mass Ejections*, *Geophysical Monograph* **89**, American Geophysical Union, Washington, 9.

Hewish, A., Scott, P.F., Wills, D.: 1964, *Nature* **203**, 1214.

Hick, P.P., Jackson, B.V.: 2004, In: Fineschi, S., Gummin, M.A. (eds.) *Telescopes and Instrumentation for Solar Astrophysics*, *Proc. SPIE* **5171**, 287 – 297. doi:10.1117/12.513122.

Howard, T.A., Fry, C.D., Johnston, J.C., Webb, D.F.: 2007, *Astrophys. J.* **667**, 610.

Hundhausen, A.J.: 1977, In: Zirker, J.B. (ed.) *Coronal Holes and High-Speed Wind Streams*, Colorado Associated University Press, Boulder, 225.

Jackson, B.V., Hick, P.P.: 2005, In: Gary, D.G., Keller, C.U. (eds.) *Solar and Space Weather Radiophysics Current Status and Future Developments*, *ASSL* **314**, Springer, Dordrecht, 355.

Jackson, B.V., Hick, P.P., Kojima, M., Yokobe, A.: 1998, *J. Geophys. Res.* **103**, 12049.

Jackson, B.V., Hick, P.P., Buffington, A., Kojima, M., Tokumaru, M., Fujiki, K., Ohmi, T., Yamashita, M.: 2003, In: Velli, M., Bruno, R., Malara, F. (eds.) *Proc. Solar Wind X*, *AIP Conf. Proc.* **679**, 75.

Jackson, B.V., Hick, P.P., Buffington, A., Bisi, M.M., Clover, J.M., Tokumaru, M.: 2010, *Adv. Geosci.* in press.

Janardhan, P., Balasubramanian, V., Ananthakrishnan, S., Dryer, M., Bhatnagar, A., McIntosh, P.S.: 1996, *Solar Phys.* **166**, 379.

Kojima, M., Fujiki, K., Ohmi, T., Tokumaru, M., Yokobe, A., Hakamada, K.: 1999, *Space Sci. Rev.* **87**, 237.

Krall, J., St. Cyr, O.C.: 2006, *Astrophys. J.* **652**, 1740.

Koutchmy, S., Slemzin, V., Filippov, B., Noens, J.-C., Romeuf, D., Golub, L.: 2008, *Astron. Astrophys.* **483**, 599.

Kubo, M., Yokoyama, T., Katsukawa, Y., Lites, B., Tsuneta, S., Suematsu, Y., Ichimoto, K., Shimizu, T., Nagata, S., Tarbell, T.D.: 2007, *Publ. Astron. Soc. Pac.* **59**, S779.

Liu, Y., Luhmann, J.G., Müller-Mellin, R., Schroeder, P.C., Wang, L., Lin, P., Bale, S.D., Li, Y., Acuã, M.H., Savaud, J.A.: 2008, *Astrophys. J. Lett.* **689**, 563.

Manoharan, P.K.: 1993, *Solar Phys.* **148**, 153.
Manoharan, P.K.: 2006, *Solar Phys.* **235**, 345.
Manoharan, P.K., Ananthakrishnan, S.: 1990, *Mon. Not. Roy. Astron. Soc.* **244**, 691.
Manoharan, P.K., Ananthakrishnan, S., Rao, A.P.: 1988, In: Pizzo, V.J., Holzer, T.E., Sime, D.G. (eds.) *Proc. of Sixth Solar Wind Conference* **I**, NCAR, Boulder, 55.
Manoharan, P.K., Kojima, M., Misawa, H.: 1994, *J. Geophys. Res.* **99**, 23411.
Manoharan, P.K., Pick, M., LASCO Consortium: 2002, In: Rao, A.P., *et al.* (eds.) *The Universe at Low Radio Frequencies, Proc. IAU Symp.* **199**, 426.
Manoharan, P.K., Ananthakrishnan, S., Dryer, M., Detman, T.R., Leinbach, H., Kojima, M., Watanabe, T., Kahn, J.: 1995, *Solar Phys.* **156**, 377.
Manoharan, P.K., Kojima, M., Gopalswamy, N., Kondo, T., Smith, Z.: 2000, *Astrophys. J.* **350**, 1061.
Manoharan, P.K., Tokumaru, M., Pick, M., Subramanian, P., Ipavich, F.M., Schenk, K., Kaiser, M.L., Lepping, R.P., Vourlidas, A.: 2001, *Astrophys. J.* **559**, 1180.
Michalek, G., Gopalswamy, N., Lara, A., Manoharan, P.K.: 2004, *Astron. Astrophys.* **423**, 729.
Mulligan, T., Russell, C.T., Anderson, B.J., Acuna, H.M.: 2001, *Geophys. Res. Lett.* **28**, 4417.
Purvis, A., Tappin, S.J., Rees, W.G., Hewish, A., Duffett-Smith, P.J.: 1987, *Mon. Not. Roy. Astron. Soc.* **229**, 589.
Selvanayagam, A.J., Praveenkumar, A., Nandagopal, D., Velusamy, T.: 1993, *IETE Tech. Rev.* **10**, 333.
Su, Y., Golub, L., van Ballegooien, A., DeLuca, E.E., Reeves, K.K., Sakao, T., Kano, R., Narukage, N., Shibasaki, K.: 2007, *Publ. Astron. Soc. Japan* **59**, S785.
Swarup, G., Sarma, N.V.G., Joshi, M.N., Kapahi, V.K., Bagri, D.S., Damle, S.H., Ananthakrishnan, S., Balasubramanian, V., Bhave, S.S., Sinha, R.P.: 1971, *Nat. Phys. Sci.* **230**, 185.
Tokumaru, M., Kojima, M., Fujiki, K., Yamashita, M., Yokobe, A.: 2003, *J. Geophys. Res.* **101**, 1220.
Torsti, J., Kocharov, L., Innes, D.E., Laivola, J., Sahla, T.: 2001, *Astron. Astrophys.* **365**, 198.
Tsurutani, B.T., Gonzalez, W.D., Gonzalez, A.L.C., Guarnieri, F.L., Gopalswamy, N., Grande, M., Kamide, Y., *et al.*: 2006, *J. Geophys. Res.* **111**, A07S01.
van Driel-Gesztelyi, L., Manoharan, P.K., Démoulin, P., Aulanier, G., Mandrini, C.H., López-Fuentes, M., Schmieder, B., Orlando, S., Thompson, B., Plunkett, S.: 2000, *J. Atmos. Solar-Terr. Res.* **62**, 1437.
Vourlidas, A., Subramanian, P., Dere, K.P., Howard, R.A.: 2000, *Astrophys. J.* **534**, 456.
Yamauchi, Y., Tokumaru, M., Kojima, M., Manoharan, P.K., Esser, R.: 1998, *J. Geophys. Res.* **103**, 6571.
Zhang, J., Richardson, I.G., Webb, D.F., Gopalswamy, N., Huttunen, E., Kasper, J.C., Nitta, N.V., Poomvises, W., Thompson, B.J., Wu, C.-C.: 2007, *J. Geophys. Res.* A10102.